optics

MDPI

Article

First-Principles Study of Electronic, Optical, and Magnetic Properties of Fe-, Co-, and Ni-Doped MoS_2 Monolayer

Soufyane Aqiqi [1], Elarbi Laghchim [2] and C. A. Duque [3,*]

[1] Department of Physics, University of Nevada Reno, Reno, NV 89502-0216, USA
[2] Materials and Subatomic Physics Laboratory, Physics Department, Ibn Tofail University, B.P. 133, Kenitra 14000, Morocco
[3] Grupo de Materia Condensada-UdeA, Instituto de Física, Facultad de Ciencias Exactas y Naturales, Universidad de Antioquia UdeA, Calle 70 No. 52-21, Medellín 050010, Colombia
* Correspondence: carlos.duque1@udea.edu.co

Abstract

In this work, a comprehensive first-principles investigation of the electronic, magnetic, and optical properties of pristine and Fe-, Co-, and Ni-doped MoS_2 monolayers is presented within the framework of density functional theory. Substitutional transition-metal doping at the Mo site is shown to induce spin-polarized impurity states within the pristine band gap, leading to significant modifications of the electronic structure, including metallic, semimetallic, or half-metallic behavior depending on the dopant species. The calculated spin-resolved band structures and projected density of states reveal a strong hybridization between the dopant 3*d* orbitals and the Mo-4*d*/S-3*p* states, giving rise to sizable magnetic moments and dopant-dependent exchange splitting. When spin–orbit coupling is included, the combined effect of exchange interactions and relativistic effects leads to an effective valley splitting at the K and K' points, whose magnitude and sign depend sensitively on the chemical nature of the dopant. Optical properties are analyzed within a linear-response framework, showing pronounced dopant-induced modifications of the optical spectra. While the pristine monolayer exhibits well-defined excitonic features, transition-metal substitution introduces low-energy optical transitions associated with impurity-related states. Consequently, the exciton binding energies estimated from the difference between the electronic and optical gaps are interpreted as effective measures of dopant-induced perturbations to optical transitions, rather than as quantitative many-body excitonic binding energies in the strict sense. These results provide microscopic insight into the interplay between magnetism, spin–orbit coupling, and optical response in doped MoS_2 monolayers, highlighting the potential of transition-metal substitution as a route to engineer spin- and valley-dependent phenomena in two-dimensional materials.

Keywords: two-dimensional material; molybdenum disulfide; density functional theory; ferromagnetic stability

Academic Editor: Tino Hofmann

Received: 21 January 2026
Revised: 6 March 2026
Accepted: 17 March 2026
Published: 23 March 2026

1. Introduction

Two-dimensional (2D) materials have received considerable attention in recent years due to their exceptional physical properties and wide-ranging applications in fields such as electronics, spintronics, catalysis, and energy storage technologies [1,2]. Among these, transition-metal dichalcogenides (TMDCs), especially molybdenum disulfide (MoS_2), are of particular interest. MoS_2 transitions from an indirect band-gap semiconductor in its bulk form to a direct band-gap semiconductor with a gap of approximately 1.8 eV in its

monolayer form, which makes it promising for applications in optoelectronics, including photodetectors, solar cells, and light-emitting devices [3]. MoS_2 also exhibits a relatively strong spin–orbit coupling (SOC) compared to other 2D materials such as graphene. This SOC enables spin–valley coupling, making monolayer MoS_2 an attractive platform for next-generation spintronic and valleytronic devices [4,5].

Spintronics is an emerging field that relies on the intrinsic spin of electrons rather than just their charge to store and process information. Devices based on spin manipulation, such as spin valves and magnetic tunnel junctions, offer potential for novel non-volatile memories and logic architectures with significantly lower power consumption than conventional charge-based electronic components. Valley electronics, on the other hand, uses an additional quantum degree of freedom: the valley index associated with the non-equivalent K and K' points in the Brillouin zone. This valley pseudospin serves as an information carrier in materials that break inversion symmetry, where strong spin–orbit coupling establishes a direct connection between the spin and valley degrees of freedom. In single-layer MoS_2, the combined effects of spin–orbit coupling and time-reversal symmetry give rise to spin–valley-locked optical selection rules. These rules enable selective optical excitation of individual valleys and direct optical readout of valley polarization [6–10].

In addition to monolayer transition-metal dichalcogenides, extensive theoretical work on semiconductor nanostructures has demonstrated that quantum confinement, impurity states, and external perturbations such as electric and magnetic fields can strongly influence excitonic behavior and optical transitions. In quantum dots and related low-dimensional systems, these factors may significantly modify exciton binding energies and absorption spectra, leading to tunable optoelectronic responses [11,12]. Similar effects have also been investigated in layered materials and heterostructures, where defects, structural modifications, and dimensionality play a crucial role in determining the electronic structure and optical properties [13,14]. Furthermore, recent theoretical analyses of multilayer quantum systems have highlighted the importance of excitonic interactions and electronic coupling in shaping the optical response of confined nanoscale materials [15]. These results provide useful conceptual insights for understanding how impurity-induced states and quantum confinement effects may modify the electronic and optical behavior of doped MoS_2 monolayers.

While the electronic and optical properties of pristine monolayer MoS_2 have been thoroughly studied experimentally and theoretically [16,17], its magnetic properties are less explored. Pristine MoS_2 is non-magnetic; however, studies have shown that magnetism can be induced through various strategies such as edge engineering, vacancy defects, and doping with transition-metal atoms [18,19]. For instance, recent work demonstrated that Fe doping enhances valley Zeeman splitting in monolayer MoS_2, attributed to the hybridization of Fe and Mo d-orbitals, resulting in a significantly increased effective g_{eff} factor compared to undoped MoS_2 [20]. The introduction of such magnetic properties into MoS_2 through doping could enable its application as a diluted magnetic semiconductor (DMS) for spintronic devices [21].

Pristine MoS_2 is intrinsically non-magnetic; however, magnetism can be induced through structural modifications such as edge engineering, atomic vacancies, and substitutional doping with transition-metal atoms [22,23]. In particular, vacancy-induced magnetism originates from defect-induced localized states that emerge within the band gap due to unsaturated bonds and reduced atomic coordination. For example, sulfur vacancies can introduce localized electronic states near the Fermi level, which may break spin degeneracy and give rise to local magnetic moments depending on their concentration and distribution. Edge terminations in finite MoS_2 flakes can similarly host localized states associated with dangling bonds, leading to spin polarization. Comprehensive reviews

have discussed the electronic, magnetic, and transport properties of vacancy defects in transition-metal dichalcogenides, as well as the practical limitations associated with vacancy engineering, including defect clustering, structural instability, and reduced carrier mobility [24,25]. These considerations show that defect-induced magnetism is fundamentally linked to localized in-gap states, distinguishing it from substitutional magnetic doping strategies explored in the present work.

Although previous studies have primarily focused on doping MoS_2 with transition metals, such as cobalt (Co), they have yielded mixed results. Some studies report that Co doping induces ferromagnetism [26,27], while others suggest antiferromagnetic or non-magnetic behavior depending on the doping concentration and the defect states present [28,29]. However, doping with other transition metals such as iron (Fe) and nickel (Ni), which also have magnetic moments, has not been comprehensively investigated.

In addition to uniform substitutional doping, recent research suggests that controlling the spatial arrangement of dopants or defects provides an additional means of modifying the electronic and functional characteristics of two-dimensional materials. For instance, the electrical structure of monolayer MoS_2 can be spatially changed by patterned distributions of defects or dopants by causing carrier transport and generating defect-related states inside the band gap. Within this type of spatial control, defect engineering can be used to tune properties such as electrical conductivity, optical response, and catalytic activity. These developments highlight how defect engineering is evolving from a simple method of property modification to a strategy for designing functional nanoscale architectures [30].

In this study, we performed first-principles density functional theory (DFT) calculations to investigate the effects of Fe, Co, and Ni doping on the electronic, optical, and magnetic properties of MoS_2 monolayers. Our primary objective was to offer comparative insight into how these dopants affect the band structure, spin polarization, and optical properties of MoS_2, thus advancing the understanding of transition metal-doped 2D materials for potential applications in spintronics and optoelectronics.

2. Methodology

First-principles calculations were performed using DFT as implemented in the Vienna Ab Initio Simulation Package (VASP) [31]. Exchange–correlation interactions were employed using the Perdew–Burke–Ernzerhof (PBE) functional in the generalized gradient approximation (GGA).

It is important to emphasize that the present calculations are primarily based on the GGA-PBE exchange–correlation functional, which is known to underestimate band gaps and, in some cases, to over-delocalize d-electrons in transition-metal systems. While GGA-PBE provides a reliable qualitative description of trends in electronic structure and magnetism, quantitative predictions of band gaps, magnetic moments, and excitonic properties may be affected by self-interaction errors. In particular, systems involving partially filled 3*d* orbitals, such as Fe-, Co-, and Ni-doped MoS_2, are especially sensitive to the choice of exchange–correlation treatment.

Nevertheless, the main objective of this work is to establish comparative trends among different dopants in a consistent theoretical framework. As demonstrated by the good agreement with previously reported experimental and GW results for pristine MoS_2, the methodology employed captures the essential physics governing the electronic and optical behavior. More accurate approaches, such as hybrid functionals or DFT + U schemes, may further refine quantitative band-gap and magnetic-moment values, particularly for Ni-doped systems, and are left for future investigations.

Spin–orbit coupling (SOC) was applied to both pristine and doped MoS_2 systems. The plane-wave cutoff energy was set to 400 eV. A $3 \times 3 \times 1$ k-point mesh based on a Monkhorst–Pack was applied for relaxation and static calculations and a Monkhorst–Pack $9 \times 9 \times 1$ grid for the density of states (DOS) calculations. The energy convergence threshold was fixed at 10^{-6} eV, and the Hellmann–Feynman force criterion for ionic relaxation between each atom was set to be -0.005 eV/Å. In these calculations, a 6×6 MoS_2 monolayer supercell structure containing 36 Mo and 72 S atoms was adopted. Structural relaxation was applied to supercells with and without defects. During the optimization process, the positions of all atoms in the supercell were fully relaxed. To prevent interaction between two neighboring periodic slabs, a substantial vacuum space of 20 Å was applied along the z-direction.

All calculations were performed using the projector augmented wave (PAW) method as implemented in VASP, with the valence configurations defined by the PAW datasets distributed with the code. Structural relaxations were performed at fixed in-plane lattice vectors of the supercell while fully relaxing all ionic positions until the maximum residual force on each atom was below 5×10^{-3} eV/Å and total energy changes were below 10^{-6} eV. Brillouin-zone integrations employed a Monkhorst–Pack mesh together with a small electronic smearing; total energies were extrapolated to the zero-smearing limit when relevant. Spin polarization was enabled for all doped configurations, and the initial local magnetic moments were assigned on the dopant site to ensure that the self-consistent solution explores the physically relevant spin-polarized manifold.

To validate the numerical stability of the reported trends, we verified that the key quantities (relative formation energies, total magnetic moments, and the presence/position of dopant-induced in-gap states) do not qualitatively change as the plane-wave cutoff and the k-point mesh are increased. In particular, test calculations with a higher cutoff and denser k-point sampling, using settings similar to those reported, were performed to confirm that the main conclusions are robust within the dilute-doping supercell approach adopted in this work.

The formation energy E_{for} of the doped MoS_2 system was calculated using the following equation, based on a previous study [32]:

$$E_{\text{for}} = E_{\text{dop}/MoS_2} + \mu_{\text{Mo}} - E_{MoS_2} - \mu_{\text{dop}}\,, \tag{1}$$

where E_{dop/MoS_2} and E_{MoS_2} are the energy of the doped and pristine MoS_2 monolayer, respectively. μ_{dop} is the chemical potential of the dopant (Fe, Co, and Ni), and μ_{Mo} is the chemical potential of a Mo atom in pristine MoS_2.

To make the definition of defect formation energy unambiguous, elemental chemical potentials were referenced to the most stable bulk phases of the corresponding elements (Mo, Fe, Co, and Ni), while respecting the thermodynamic stability condition for the MoS_2 host. In practice, the allowed range of μ_{Mo} and μ_{S} is bounded by $\mu_{\text{Mo}} + 2\mu_{\text{S}} = \mu_{MoS_2}$, with the Mo-rich (S-poor) limit obtained by setting μ_{Mo} to bulk Mo and the S-rich (Mo-poor) limit obtained by setting μ_{S} to its elemental reference. The formation energies reported here correspond to a consistent choice of reservoir conditions, enabling a meaningful comparison across Fe, Co, and Ni substitutions on the Mo site within the same supercell framework.

Similarly to the formation energy E_{for}, the charge density difference of absorption systems was calculated by

$$\Delta_\rho = \rho_{\text{dop}/MoS_2} - \rho_{MoS_2} - \rho_{\text{dop}}\,, \tag{2}$$

where ρ_{dop/MoS_2} represents the charge density of the doped MoS_2 monolayer and ρ_{MoS_2} refers to the charge density of the pristine MoS_2 monolayer. In contrast, ρ_{dop} represents

the charge density of the dopant elements (Fe, Co, and Ni). For pristine MoS_2, the exciton binding energy E_b was estimated using the difference between the fundamental band gap E_g and the optical band gap E_{opt} [33]:

$$E_b = E_g - E_{\text{opt}}\,. \tag{3}$$

While this relation provides a meaningful estimate of exciton binding energy for pristine monolayer MoS_2 where well-defined band-edge excitons exist, its interpretation in doped supercells requires special care. In Fe-, Co-, and Ni-doped systems, substitutional impurities introduce localized in-gap states and, in some cases, a finite density of states near the Fermi level. Consequently, the lowest optical transitions may occur between defect-related states rather than between extended valence- and conduction-band states. In such cases, E_g corresponds to the energy separation between defect-related levels, and E_{opt} represents the lowest allowed defect-related excitation. Therefore, the quantity $E_b = E_g - E_{\text{opt}}$ should be interpreted as an effective measure of defect-induced optical re-normalization rather than as a conventional Wannier–Mott exciton binding energy.

For doped supercells, we denote with E_{opt} the *optical onset* extracted from the first allowed transitions in the calculated spectrum. Because Fe/Co/Ni substitution introduces impurity-derived in-gap states and can yield a finite density of states near E_F, the lowest-energy optical transitions may involve defect-related states rather than delocalized band-edge electron–hole pairs. Therefore, in doped systems, the quantity $E_b = E_g - E_{\text{opt}}$ should be interpreted as an *effective transition-energy difference* within the same computational protocol, not as a quantitatively predictive many-body exciton binding energy.

To obtain optical excitations, we employed a linear-response TD-DFT approach in the periodic supercell transition basis, as detailed below. This approach captures excitonic effects beyond the independent particle approximation. The excitation energies were calculated by solving the Casida equations, which are expressed as [34]:

$$\Sigma_{q'} W_{qq'}(\Omega) \nu_{q'} = \Omega^2 \nu_q \tag{4}$$

and

$$W_{qq'}(\Omega) = \omega_q^2 \delta_{qq'} + 4\sqrt{\omega_q \omega_{q'}}\, M_{qq'}(\Omega)\,, \tag{5}$$

where ω_q and $\omega_{q'}$ are the differences between the occupied and unoccupied Kohn–Sham orbitals, $M_{qq'}$ is the coupling matrix involving the Hartree and the exchange–correlation kernel, and Ω denotes the excitation energies.

In the present work, optical excitations are obtained within a linear-response TD-DFT framework formulated in a discrete basis of Kohn–Sham single-particle transitions of the periodic supercell. Within this transition-space representation, the response reduces to solving a Casida-like eigenvalue problem for the excitation energies Ω. We stress that this procedure is applied to the *periodic slab supercell* (large in-plane cell and large vacuum) and is used here primarily to establish *comparative trends* in the optical onset and spectral redistribution induced by Fe/Co/Ni substitution, rather than to provide fully quantitative exciton energies for an extended bulk crystal. Consequently, effects such as quasiparticle self-energy corrections (GW) and a fully predictive treatment of electron–hole interactions in the presence of metallic/impurity resonances (e.g., GW + BSE) are beyond the scope of the present study and are left for future work.

The effective KK' valley splitting $\Delta KK'$ is defined as [35]:

$$\Delta KK' = \Delta CB - \Delta VB\,, \tag{6}$$

where ΔCB and ΔVB are the energy shifts of the conduction and valence bands.

The quantities Δ_{VB} and Δ_{CB} were obtained by explicitly comparing the SOC-included band-edge energies at the K and K' valleys for the relevant spin-split branches. In practice, after self-consistent SOC calculations, we identified the valence-band maximum and conduction-band minimum at K and K' and tracked their spin-resolved counterparts by continuity of the band dispersion and orbital character. The reported effective valley splitting $\Delta_{KK'} = \Delta_{CB} - \Delta_{VB}$ therefore reflects the combined action of SOC and dopant-induced exchange fields that break time-reversal symmetry in the doped supercells. This procedure ensures that both the magnitude and sign of $\Delta_{KK'}$ are consistently defined across Fe, Co, and Ni substitutions.

3. Result and Discussion

3.1. Crystal Properties

3.1.1. Atomic Configurations of the Defect in MoS_2

This study focuses on the effect of substituting Fe, Co, and Ni atoms into a monolayer of MoS_2 on its electronic, optical, and magnetic properties. To simulate doping, a single Mo atom in a $6 \times 6 \times 1$ supercell was replaced by a transition-metal atom (Fe, Co, or Ni), corresponding to a dopant concentration of approximately 2.8%. The substitutional doping mechanism involves the introduction of the dopant atom at a Mo vacancy site, effectively replacing one molybdenum atom in the lattice.

This approach preserves the integrity of the MoS_2 hexagonal structure while inducing localized changes in the electronic environment due to the different electronic configurations and magnetic moments of the transition-metal dopants. Relaxed atomic configurations show that the dopant atoms (Fe, Co, and Ni) are stably accommodated within the MoS_2 lattice with slight local distortions in the surrounding sulfur atoms. These distortions arise due to the differences in atomic radii and bonding characteristics between Mo and the dopant atoms. This structural adjustment plays a crucial role in the modification of the electronic band structure, charge distribution, and magnetic interactions in the doped systems.

3.1.2. Properties of Pristine MoS_2

Figure 1a illustrates the atomic structure of a monolayer MoS_2, which consists of three atomic layers. These layers consist of one layer of molybdenum (Mo) atoms sandwiched between two layers of sulfur (S) atoms, arranged in a trigonal prismatic pattern. In its pristine form, monolayer MoS_2 has a direct band gap, where the conduction-band minimum (CBM) and valence-band maximum (VBM) are located at the K-point of the Brillouin zone. The average Mo-S bond length was approximately 2.43 Å, consistent with the experimental and theoretical values reported. We used a vacuum spacing of 20 Å along the z-direction to avoid the interaction between the monolayers and their periodic images. The GGA-PBE method was used to optimize the lattice constant of monolayer MoS_2. At equilibrium, the calculated lattice constant was 3.19 Å, which is in good agreement with previous work [36]. The calculated partial density of states (PDOS) for the supercell reveals a band gap of 1.6 eV for the pristine monolayer MoS_2, which aligns well with the previously reported value of 1.65 eV [37]. The slight underestimate is attributed to the GGA-PBE approach, which tends to underestimate band gaps because of the lack of quasiparticle corrections. These baseline results for pristine MoS_2 establish a reference to understand the modifications induced by transition-metal doping, which are discussed in the following sections.

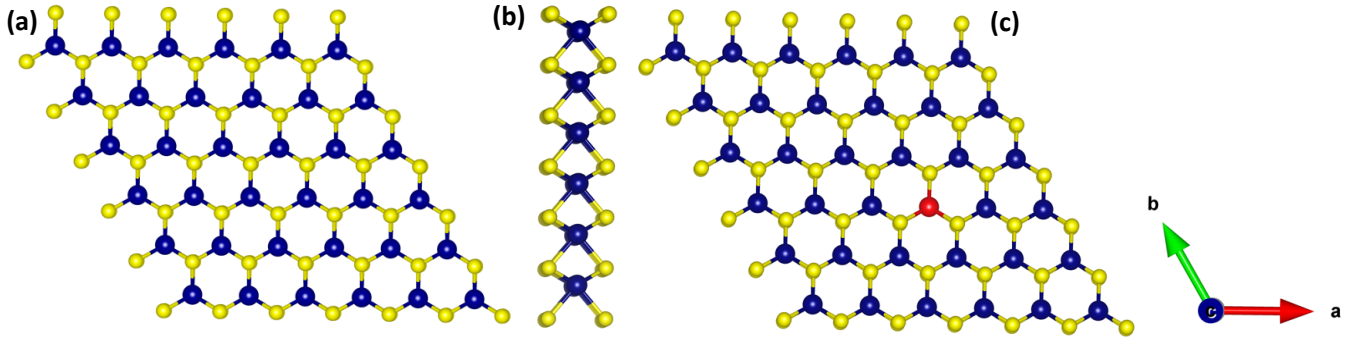

Figure 1. (**a**) Top and (**b**) side views of the atomic structure of the MoS_2 monolayer, (**c**) with Fe, Ni, and Co substituting the Mo site. The blue, yellow, and red balls represent Mo, S, and the dopant atoms (Fe, Co, and Ni), respectively.

3.1.3. Formation Energy

An analysis of the calculated formation energies of dopant incorporation into the MoS_2 monolayer provides insights for the stability and energy characteristics of these doped systems, revealing patterns among the different transition-metal dopants. Table 1 summarizes the calculated formation energies for Fe-, Co-, and Ni-doped MoS_2 systems. Fe-doped MoS_2 exhibits the lowest formation energy of 3.11 eV, indicating that Fe atoms are reasonably easy to incorporate into the MoS_2 lattice. This suggests that Fe doping is more energetically favorable, providing a stable substitutional configuration compared to Co and Ni doping. The formation energy exhibits a gradual rise when we move across the 3d transition-metal series from Fe to Co to Ni in the periodic table. The formation energy of Co-doped MoS_2 is measured to be 4.32 eV, suggesting that the process of incorporating cobalt atoms into the MoS_2 lattice takes a somewhat higher amount of energy compared to iron doping. In particular, this value is in good agreement with previous results that report an absolute formation energy of 4.64 eV for Co-doped MoS_2 [38]. Finally, Ni-doped MoS_2 has a formation energy of 4.94 eV, indicating that adding nickel atoms to the MoS_2 structure is less energetically beneficial than doping with Co and Fe. This trend reflects the influence of the atomic size and electronic configuration of the dopant atoms, which affect the lattice distortion and bonding energetics upon substitution. These patterns demonstrate how the location of the dopant in the periodic table affects the stability and the possibility of doping in MoS_2. This information helps to design and optimize materials for different applications. The increasing formation energy trend correlates with the rising atomic number and decreasing tendency for orbital hybridization with Mo and S atoms in the host lattice. These results agree with previous theoretical investigations on transition-metal doping in TMDCs, where early 3d dopants typically exhibit stronger binding and enhanced lattice compatibility [39]. The formation energies provide valuable information on the feasibility of synthesis and the probability of successful incorporation of each element under experimental conditions. Therefore, Fe stands out as the most suitable candidate for substitutional doping in MoS_2 among the three, not only because of its favorable energetics but also in terms of material design for spintronic and catalytic applications.

Table 1. Formation energy for the doped MoS_2 monolayer in eV.

	Fe-MoS_2	**Co-MoS_2**	**Ni-MoS_2**
Formation Energy	3.11	4.32	4.94

3.2. Electronic Structure

3.2.1. Band Structures

An analysis was performed to examine the electronic band structure of the doped systems and compare it with that of the pristine MoS_2 monolayer. Figure 2 illustrates the electronic band structures of the pristine and the doped MoS_2 monolayer.

The presence of a dopant in the form of Fe, Co, and Ni atoms results in impurity states that are located in proximity to the top of the valence band. This indicates that the doping process is of the *p*-type nature.

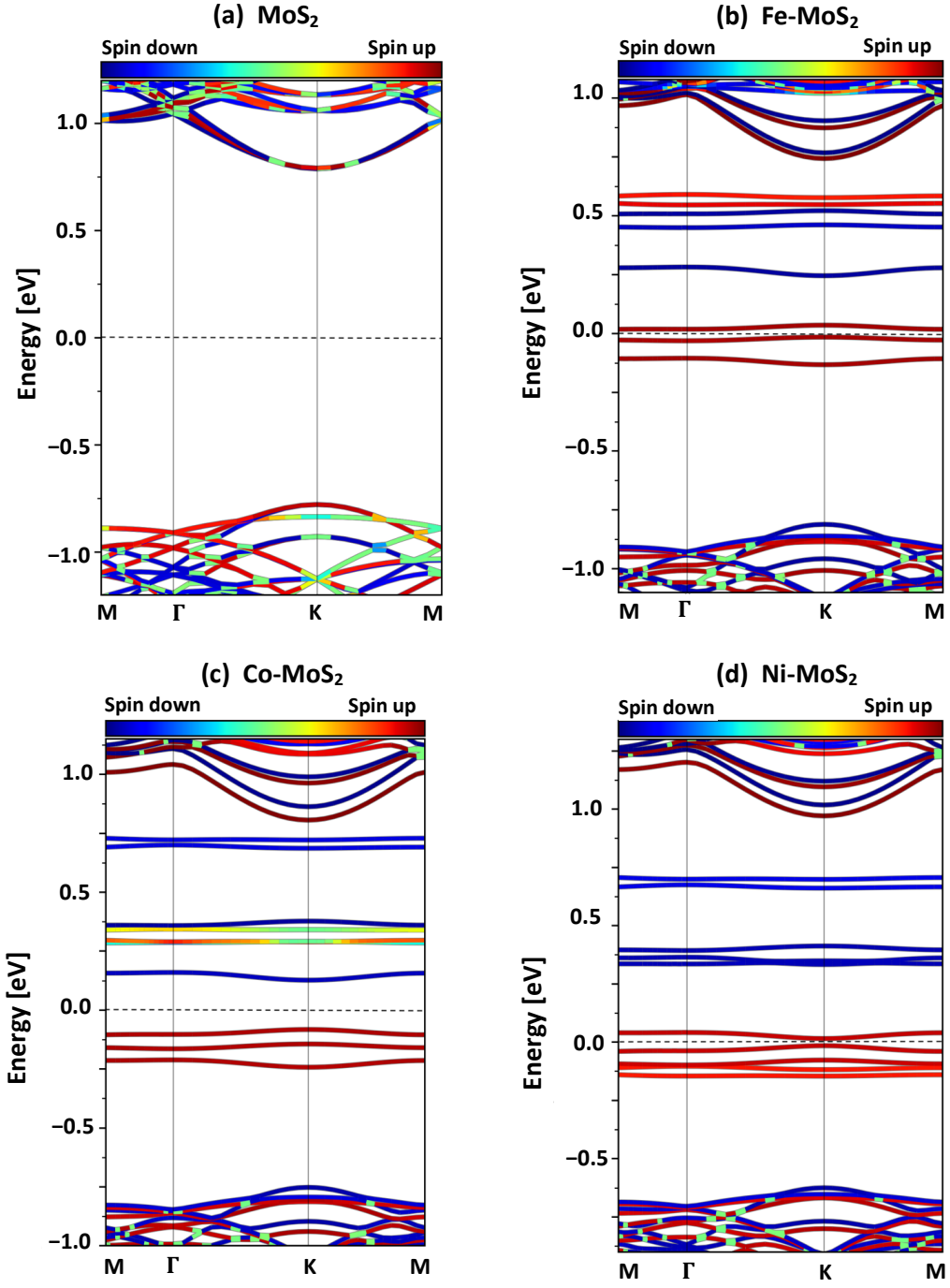

Figure 2. The electronic band structure calculated along the high-symmetry direction for the pristine and doped MoS_2 monolayer [40]. The dotted line shows the Fermi energy level.

To avoid ambiguity arising from electronic character induced by substitutional Fe/Co/Ni at the Mo site, we emphasize that the relevant indicators are the position of the Fermi level and the occupation of dopant-derived states. In the present supercell calculations, the dopant introduces spin-polarized 3*d*-dominated states within the pristine gap and near the band edges. Depending on their occupation, these states can pin E_F and yield metallic or half-metallic behavior in one spin channel, rather than a simple textbook "*p*-type" scenario. Therefore, we interpret the calculated spectra primarily as evidence of dopant-induced in-gap resonances and Fermi-level pinning, and we discuss the electronic character in terms of the resulting density of states at E_F and the spin-resolved band crossings. This dopant-induced pinning of E_F and the emergence of in-gap resonances naturally imply that the lowest optical transitions in doped systems can occur at very low energies and need not correspond to pristine-like band-edge excitons.

The Co-doped MoS_2 exhibits the formation of two impurity energy levels positioned around 0.72 eV and 0.68 eV below the CBM. In Ni-doped MoS_2, two impurity energy levels emerge around 0.70 eV and 0.66 eV below the CBM. Similarly, MoS_2 doped with iron (Fe) shows two impurity energy levels. These levels are positioned at roughly 0.58 eV and 0.55 eV below the CBM. Furthermore, the direct band gap decreases and a half-metallic character can be observed [41] in specific doped systems. This is attributed to impurity states present near the Fermi level.

Throughout this work, we use the term *half-metallic* only when the spin-resolved electronic structure exhibits a finite density of states at the Fermi level in one spin channel. At the same time, the opposite spin channel remains gapped around E_F. In contrast, we use *semimetallic*/semimetallic to indicate that both spin channels contribute states at E_F (or that the band edges overlap). This operational definition links the qualitative classification directly to the calculated spin-resolved band structures and PDOS, providing a consistent basis for comparing Fe-, Co-, and Ni-substituted MoS_2 within the same computational setup.

3.2.2. The Partial Density of States (PDOS)

To better understand the nature of the impurity states, we calculated the PDOS of the doped MoS_2 monolayers and compared it with that of the pristine MoS_2 monolayer. To determine the band gap and the position of the electronic states from the impurity atoms in the doped systems, we aligned the Fermi level to zero energy, as indicated by the black dotted line. Figure 3 shows the PDOS for a pristine and doped MoS_2 monolayer. We can see that the pristine MoS_2 is a non-magnetic semiconductor with a direct band gap of approximately 1.6 eV. An analysis of PDOS in the Co-doped MoS_2 system offers vital insights into the source of the gap states. Our calculation shows that the electrical structure is greatly affected by the presence of the Co dopant. The PDOS profiles demonstrate that the gap states predominantly originate from the d-orbitals of the Co dopant atom, emphasizing their significant impact on the electronic characteristics of the material. In addition, hybridization contributions come from the 4d-orbitals of neighboring Mo atoms and the 3p-orbitals of adjacent S atoms. The d-orbitals of the Mo atoms and the p-orbitals of the S atoms have essential influences on the formation of the electronic band structure. This strong hybridization underscores the role of the Co dopant in inducing spin polarization across the lattice.

In addition to the analysis of Co-doped MoS_2, we expanded our investigation to include PDOS analysis for Ni-doped MoS_2. Interestingly, our research showed similar hybridization effects. The orbitals have a comparable impact on the electrical structure, but their intensity is slightly lower compared to the Co-doped system near the Fermi level. The gap states are again dominated by Ni 3d orbitals, accompanied by polarization

effects in nearby Mo and S atoms. Finally, we explored the electronic structure of Fe-doped MoS_2. The PDOS reveals significant contributions from the d-orbitals of the Fe dopants and Mo atoms, whereas the involvement of the p-orbitals of the S atoms was minimal. Intriguingly, we observed the presence of gap states within the Fermi level, suggesting potential alterations in the material's conductivity and optical properties. These findings offer additional information on the nuanced effects of different dopants on the electronic behavior of MoS_2.

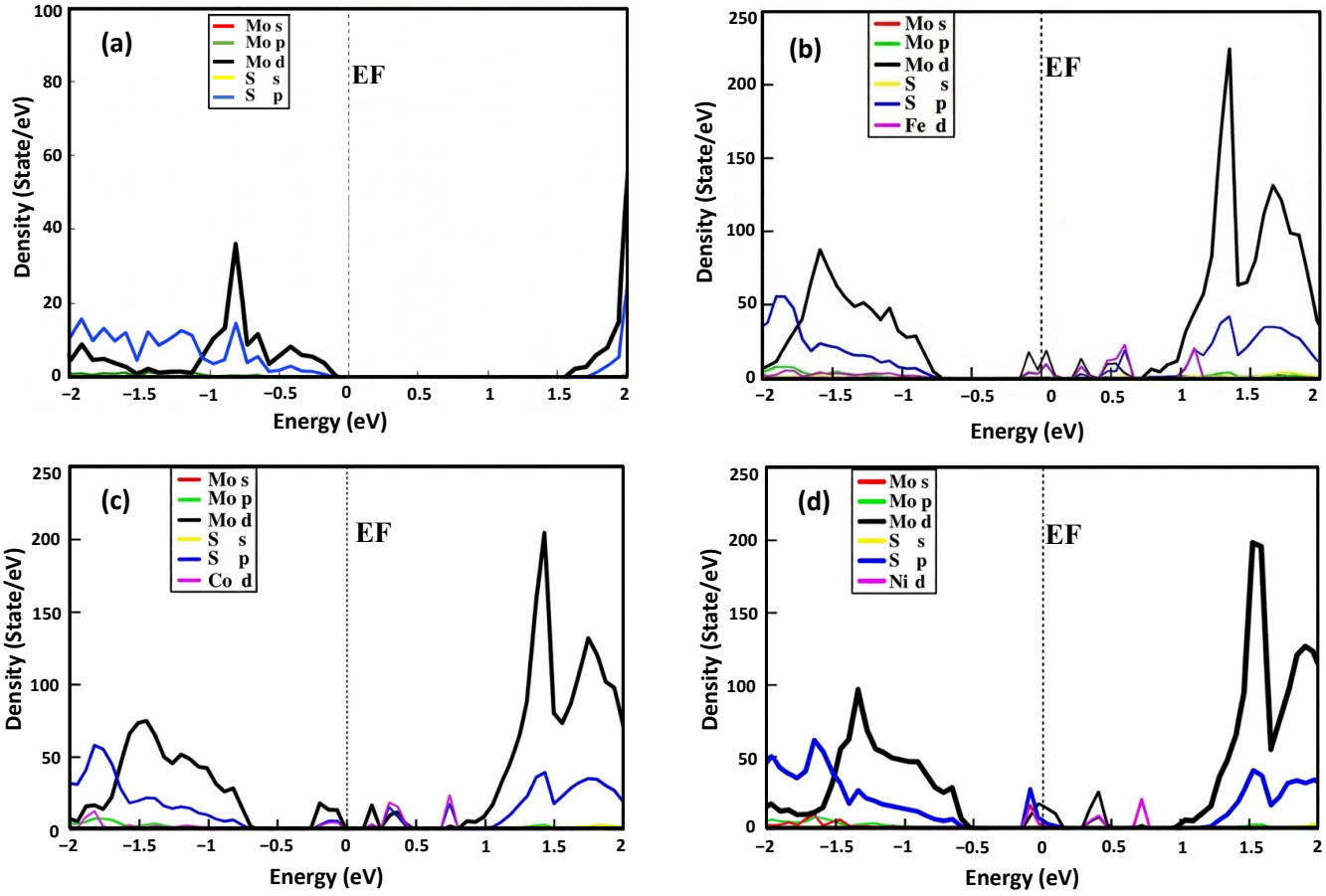

Figure 3. Partial density of states of (**a**) MoS_2 monolayer, (**b**) Fe-MoS_2, (**c**) Co-MoS_2, and (**d**) Ni-MoS_2.

3.2.3. Valley Splitting

Now, let us look over the valley splitting, as shown in Figure 4. In the doped MoS_2 monolayer, both the valence band (VB) and conduction band (CB) undergo division into two sub-bands: one for spin-up and another for spin-down electrons. Specifically, in the *K*-valley, the VB and the CB separate into VB1 and VB2, as well as CB1 and CB2, respectively. However, CB1′ (CB2′) and VB1′ (VB2′) are bands in the *K*′-valley. The splitting of VB and CB with different spins is depicted by ΔVB and ΔCB, as shown in Figure 4.

The valence band maximum (VBM) in Fe-doped MoS_2 shows a substantial splitting of around 49.5 meV due to the dopant defect with the spin–orbit coupling (SOC) and the lack of inversion symmetry. In addition, the conduction band minimum (CBM) near the *K*-point undergoes a minor splitting of 24.3 meV. The valley splitting for Fe-doped MoS_2 results in −32.1 meV. In Co-doped MoS_2, the VBM shows a separation of 52.5 meV, while the CBM at the *K*-point shows a separation of 56.9 meV. The effective valley splitting for Co-doped MoS_2 is 4.4 meV. In Ni-doped MoS_2, the VBM exhibits a separation of 43.1 meV. Additionally, the CBM at the *K*-point displays a splitting of 46.9 meV. These values are summarized in Table 2.

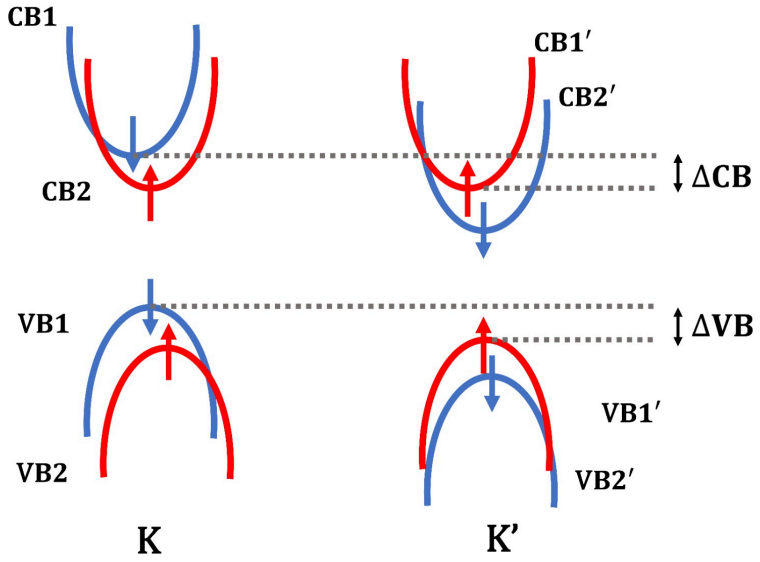

Figure 4. Schematic diagram of the KK'-valley splitting of the doped MoS_2 monolayers.

Table 2. Valley splitting of the conduction and the valence band of the pristine and doped MoS_2 monolayer near the *K*-point.

	MoS_2	Fe-MoS_2	Co-MoS_2	Ni-MoS_2
CB splitting ΔCB (meV)	0	24.3	56.9	46.9
VB splitting ΔVB (meV)	0	49.5	52.5	43.1
Valley splitting $\Delta KK'$ (meV)	0	−32.1	4.4	3.8

The observed KK'-valley splitting in doped MoS_2 arises from the combined effect of spin–orbit coupling and the exchange interaction introduced by magnetic dopants, which breaks time-reversal symmetry. In pristine MoS_2, time-reversal symmetry enforces valley degeneracy; however, substitutional Fe, Co, and Ni atoms introduce localized magnetic moments that lift this degeneracy through exchange-induced spin splitting. The magnitude and sign of effective valley splitting depend sensitively on the relative contributions of conduction- and valence-band shifts, as reflected in the calculated values ΔCB and ΔVB.

These results are consistent with previous theoretical models of magnetic proximity and exchange-driven valley polarization in two-dimensional materials, where the interplay between SOC and dopant-induced magnetism governs valley-selective energy shifts. The relatively small net valley splitting observed for Co- and Ni-doped systems indicates partial compensation between conduction- and valence-band contributions, whereas Fe doping leads to a larger asymmetry.

3.2.4. The Charge Density Difference

As shown in Figure 5, the charges at the dopant site tend to become less localized as we transition from iron doping to nickel doping. This is because nickel doping is more conductive than iron doping. The lower influence of intense on-site Coulombic interactions, which are present in elements belonging to the d-block atomic structure, is the cause of this diminishing localization.

The charge density difference maps primarily reflect how the dopant 3*d* manifold hybridizes with the neighboring Mo-4*d* and S-3*p* states and how charge is redistributed

upon substitution. Consequently, differences in the apparent spatial extent of $\Delta\rho(\mathbf{r})$ across Fe, Co, and Ni substitutions should be interpreted in terms of (i) dopant–ligand covalency and (ii) the occupancy and energetic alignment of the dopant-derived in-gap resonances, rather than as a direct proxy for "conductivity". A more quantitative assessment can be obtained by complementing $\Delta\rho(\mathbf{r})$ with an integrated charge-transfer analysis (e.g., Bader partitioning) and by comparing projected *d*-orbital occupations, which together clarify the degree of localization and the direction of charge transfer in each doped configuration.

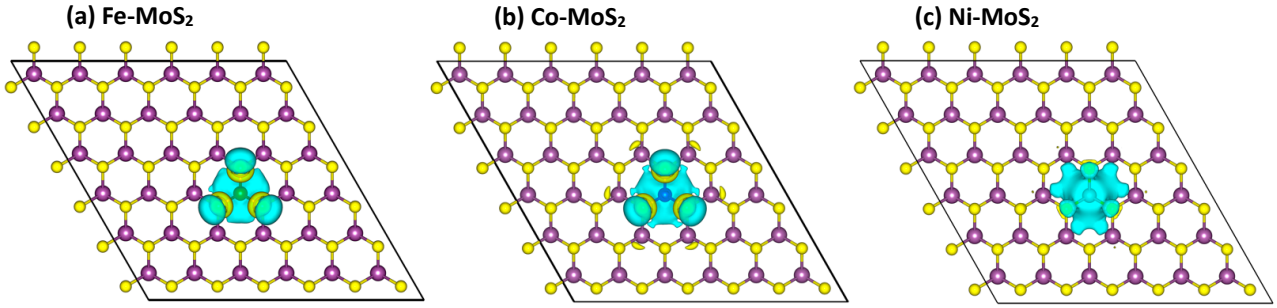

Figure 5. Charge density difference of the doped MoS_2 monolayer. The purple and yellow balls represent Mo and S atoms, respectively. The dopant atoms (Fe, Co, Ni) occupy substitutional Mo sites. The Cyan and yellow isosurfaces correspond to regions of charge accumulation and depletion, respectively.

3.3. Optical Properties

3.3.1. Photoluminescence

Optical excitation energies were obtained within a linear-response framework applied to periodic supercells, using a well-defined set of unoccupied bands, a consistent broadening parameter, and a converged Brillouin-zone sampling appropriate for optical spectra. In particular, we ensured that the calculated optical peaks and the extracted optical gap E_{opt} were numerically stable with respect to the number of empty states included in the response calculation. When SOC was enabled, the response was evaluated relative to the SOC-included ground state to capture the spin-split band-edge structure relevant to A/B excitons in pristine MoS_2.

For clarity, all auxiliary parameters entering the optical excitation model are explicitly defined. Here, ε denotes the effective dielectric screening used to mimic the environment of the monolayer. At the same time, the remaining parameters control the regularization/broadening used to extract peak positions from the calculated spectra. We note that these parameters do not alter the qualitative trends among dopants reported here but can influence the absolute values of E_{opt}; therefore, we keep them fixed across pristine and doped systems to allow for a consistent comparative analysis.

Figure 6 shows photoluminescence spectra for pristine and doped MoS_2 monolayers. It is well known that the MoS_2 monolayer is a direct band-gap semiconductor. The pristine MoS_2 monolayer displays two large, distinct peaks. These respective peaks correspond to the excitonic characteristics, referred to as A and B excitons. The two excitons are bright, with a higher energy of 1.91 eV and 2.12 eV, respectively. When Fe, Co, and Ni atoms doped MoS_2, more excitons appeared, and the excitons' intensity became weaker. We also discovered that the lowest-energy excitons are dark and more exciton peaks are bright. This is due to the effect of Fe, Co, and Ni atoms on electronic band structures.

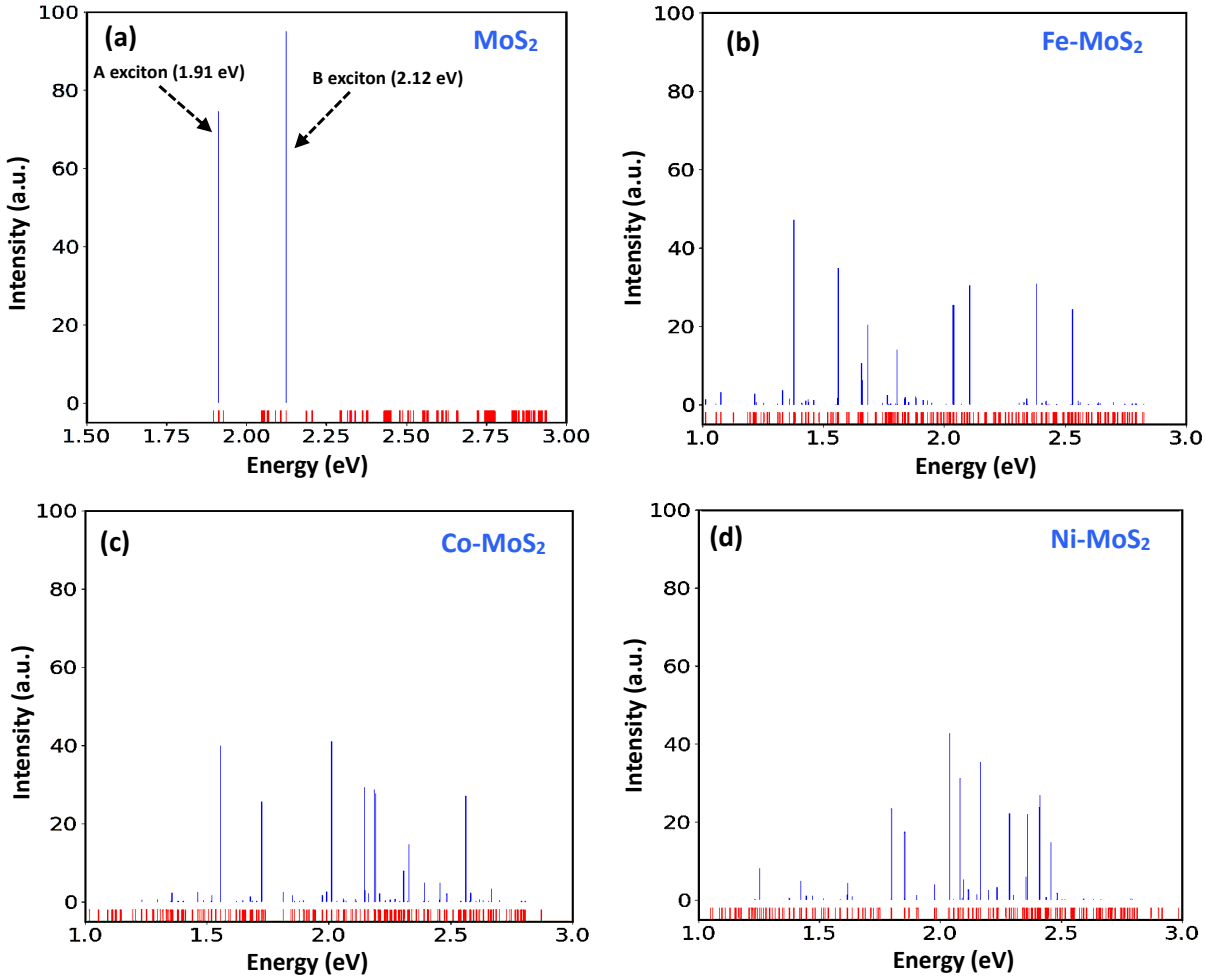

Figure 6. Photoluminescence spectra for (**a**) pristine MoS_2 monolayer, (**b**) Fe-MoS_2, (**c**) Co-MoS_2, and (**d**) Ni-MoS_2. The blue lines represent the calculated optical transition intensities, while the red ticks indicate the corresponding transition energies.

3.3.2. Binding Energy

We use the MoS_2 monolayer as an example, for which experimental and theoretical data are available for comparison. As the first validation of the theoretical framework, we compute the fundamental gap E_g and optical gap E_{opt} of the MoS_2 monolayer using TD-DFT. The gap values agree very well with the experimental a GW results, as shown in Table 3, indicating the reliability of the TD-DFT method for the systems. The exciton binding energy is estimated to be 0.77 for the MoS_2 monolayer, confirming the strong excitonic effect. In contrast, the binding energies of Fe-, Co-, and Ni-doped MoS_2 are recorded as 1.11 eV, 1.68 eV, and 0.88 eV, respectively.

According to the results of this study, the incorporation of transition-metal dopants has a considerable impact on the binding energy of MoS_2. In doped configurations, the small values of E_{opt} (e.g., 0.07 eV for Co–MoS_2) indicate that the lowest optical transitions are dominated by impurity-related states introduced by the dopant, in line with the appearance of dopant-derived in-gap resonances in the spin-resolved band structures and PDOS. Accordingly, the differences $E_b = E_g - E_{\text{opt}}$ reported in Table 3 should be viewed as *effective indicators* of the dopant-induced redistribution of low-energy optical transitions within a fixed TD-DFT protocol, rather than as quantitative exciton binding energies in the strict quasiparticle (GW) plus electron–hole (BSE) sense. For pristine MoS_2, where well-defined bright A/B excitons exist and the optical onset is associated with band-edge transitions, $E_b = E_g - E_{\text{opt}}$ retains its usual interpretation as an exciton binding-energy estimate.

Table 3. The calculated fundamental gap (E_g), optical gap (E_{opt}), and exciton binding energy (E_b) for MoS_2, Fe-MoS_2, Co-MoS_2, and Ni-MoS_2 monolayers using the TD-DFT method. All energies are in eV.

		TD-DFT $\varepsilon = 3.5; arph = 0.2; r = 0.15$	**GW**	**Experiment**
MoS_2	E_g	2.67	2.67 [42]	1.85–1.90 [43]
	E_{opt}	1.90	2.04 [42]	
	E_b	0.77	0.63 [42]	
Fe-MoS_2	E_g	1.25	—	—
	E_{opt}	0.14	—	—
	E_b	1.11	—	—
Co-MoS_2	E_g	1.75	—	—
	E_{opt}	0.07	—	—
	E_b	1.68	—	—
Ni-MoS_2	E_g	1.17	—	—
	E_{opt}	0.29	—	—
	E_b	0.88	—	—

Although the TD-DFT framework shows excellent agreement with the experimental and GW data for pristine MoS_2, its application to doped systems must be interpreted with caution. Transition-metal doping introduces mid-gap and impurity states that significantly alter screening and excitonic interactions. As a result, the extremely small optical gaps observed in doped systems should be regarded as qualitative indicators of strong electronic perturbation rather than as quantitatively predictive values.

Despite these limitations, TD-DFT remains a valuable tool for capturing relative changes in excitonic behavior induced by different dopants within a consistent computational scheme. The trends reported here highlight how Fe, Co, and Ni substitutions modify electron–hole interactions in MoS_2, offering valuable insights for future studies employing more advanced many-body approaches.

3.4. Magnetic Properties

3.4.1. Magnetic Moment

Note that the present study focuses on the magnetic moments induced by isolated substitutional dopants in a large supercell, corresponding to the dilute-doping regime. In this context, the emergence of a finite magnetic moment reflects the formation of localized magnetic states rather than long-range magnetic ordering. A rigorous demonstration of ferromagnetic or antiferromagnetic stability would require total-energy comparisons between different magnetic configurations involving multiple dopants, which is beyond the scope of the current work.

Consequently, the term "ferromagnetic stability" used in this study refers to the robustness of spin-polarized solutions at the single-dopant level under spin–orbit coupling, rather than to macroscopic long-range ferromagnetism. These results nevertheless provide an essential microscopic foundation for understanding how transition-metal dopants can act as magnetic centers in MoS_2-based diluted magnetic systems.

To investigate the influence of transition-metal dopants on the magnetic properties of monolayer MoS_2, we calculated the total magnetic moment for both pristine and doped systems (Fe, Co, and Ni). As expected, the pristine MoS_2 monolayer exhibits a non-magnetic state, with a total magnetization of 0.00 μB. This result aligns with previous theoretical studies, which have shown that the absence of net magnetization in pristine MoS_2 arises from the balance between the spin-up and spin-down states due to its symmetric electronic

structure [44]. Upon substitutional doping at the Mo site with a transition metal, magnetic moments arise, with magnitudes that depend on the type of dopant. As shown in Table 4, the Co-doped MoS_2 system displays a total magnetic moment of 2.99 μB, in excellent agreement with previous theoretical studies [37]. Furthermore, our calculations reveal a localized magnetic moment of 0.95 μB on the Co atom, consistent with prior findings on substitutional doping-induced magnetism in MoS_2.

Table 4. Magnetic moment of the dopant (Fe, Co, and Ni) and total magnetic moment for the 6 × 6 pristine and doped MoS_2 monolayers.

	Magnetic Moment of the Dopant (μB)	Total Magnetic Moment (μB)
MoS_2	~	0.00
Fe-MoS_2	1.20	1.99
Co-MoS_2	0.95	2.99
Ni-MoS_2	1.24	3.98

Using the Co-doped case as a validated benchmark, we proceeded to analyze Fe and Ni doping. For Fe-doped MoS_2, a total magnetization of 1.99 μB was obtained, which is reasonably in line with the reported values for Fe substitution in similar TMDC systems [45]. Moreover, Ni-doped MoS_2 exhibited the highest total magnetization of 3.98 μB. However, a closer inspection revealed that the local magnetic moment on the Ni atom was approximately 1.24 μB. The high magnetic moment reported for Ni is likely overestimated because localized magnetic moments are unrealistically enhanced in the absence of a sufficient description of orbital hybridization or charge redistribution. Further refinement, including hybrid functional or DFT + U calculations, may be necessary to obtain a more accurate assessment of Ni-induced magnetism. Our results provide vital insight into the significant impact of dopants on the magnetic characteristics of the MoS_2 monolayer, offering valuable insights for further exploration and potential applications in spintronics and magnetics.

3.4.2. The Spin Densities

In the present study, we also examined the impact of the dopants (Fe, Co, and Ni) on the spin-polarized state. Figure 7 presents the spin density of a MoS_2 monolayer with a single substitution of Fe, Co, and Ni at the Mo site. Most of the spins in Fe-doped MoS_2 are concentrated in the Fe atom and its surrounding Mo atoms. In contrast, for Co- and Ni-doped MoS_2, some of the spin densities are localized at the Co and Ni atoms, respectively. The doping atoms are coupled to the spins of the six nearby Mo atoms.

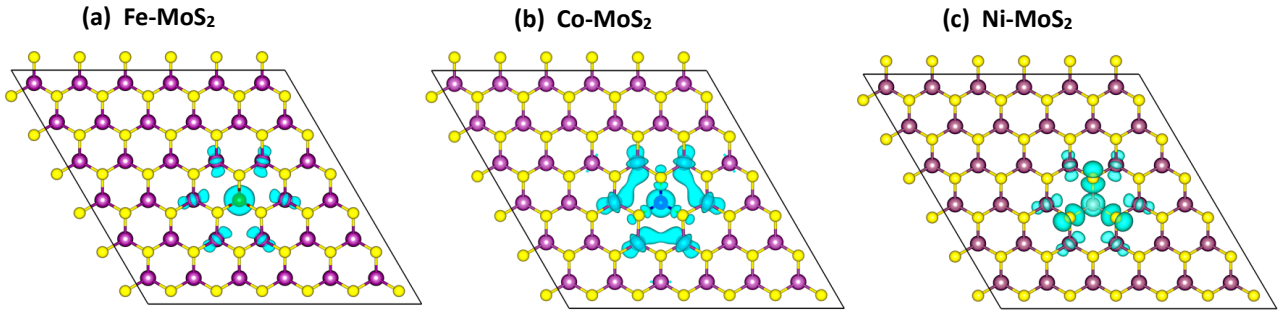

Figure 7. Spin densities in a 6 × 6 MoS_2 monolayer with three different Mo site substitutions: (**a**) Fe substitution, (**b**) Co substitution, and (**c**) Ni substitution. The purple and yellow balls represent Mo and S atoms, respectively. The cyan isosurfaces indicate regions of spin density.

4. Conclusions

In conclusion, we examined the electrical, optical, and magnetic characteristics of both pristine and doped MoS_2 monolayers by using DFT and TD-DFT. The band structures and the partial density of states were investigated. The binding and formation energies were calculated. We observed substantial modifications to the electronic band structure, including the formation of impurity bands within the band gap. We also found that the pristine MoS_2 monolayer does not exhibit a spin-polarized state. However, substitutions of Fe, Co, and Ni at the Mo site give rise to a magnetic moment and introduce localized states. The magnetic moment originates from the d-orbitals of the Fe, Co, and Ni atoms, as well as the d-orbitals of the Mo atoms and the p-orbitals of the S atoms through p-d hybridization. Moreover, our analysis of excitonic characteristics via photoluminescence reveals distinctive peaks corresponding to A and B excitons, shedding light on the optical properties of the magnetic-doped MoS_2 monolayer. Our results provide an opportunity to explore the doping of 2D transition-metal dichalcogenides, which can facilitate the development and enhancement of doped MoS_2 materials for various applications.

Finally, it is essential to recognize the limitations inherent in the present theoretical framework. The use of GGA-PBE and single-dopant supercells restricts the quantitative accuracy of band gaps, magnetic moments, and excitonic energies, particularly in systems involving localized *d*-electrons. Nevertheless, the consistent comparative analysis performed here provides a robust qualitative understanding of how Fe, Co, and Ni dopants influence the electronic, optical, and magnetic properties of MoS_2 monolayers. These results serve as a solid foundation for future studies employing more advanced exchange–correlation treatments and multi-dopant configurations.

Author Contributions: Conceptualization, S.A. and E.L.; methodology, S.A. and E.L.; software, S.A.; validation, S.A.; formal analysis, S.A. and C.A.D.; investigation, S.A. and C.A.D.; writing—original draft preparation, S.A.; writing—review and editing, C.A.D. All authors have read and agreed to the published version of the manuscript.

Funding: This research received no external funding.

Data Availability Statement: The original contributions presented in this study are included in the article. Further inquiries can be directed to the corresponding author.

Acknowledgments: C. A. Duque is grateful to Colombian agencies and CODI—Universidad de Antioquia (Estrategia de Sostenibilidad de la Universidad de Antioquia and project "Nanoestructuras semiconductoras con simetría axial basadas en InAs y GaAs para aplicaciones en electrónica ultra e híper rápida").

Conflicts of Interest: The authors declare no conflicts of interest.

References

1. Xu, M.; Liang, T.; Shi, M.; Chen, H. Graphene-like two-dimensional materials. *Chem. Rev.* **2013**, *113*, 3766–3798. [CrossRef]
2. Butler, S.Z.; Hollen, S.M.; Cao, L.; Cui, Y.; Gupta, J.A.; Gutierrez, H.R.; Heinz, T.F.; Hong, S.S.; Huang, J.; Ismach, A.F.; et al. Progress, challenges, and opportunities in two-dimensional materials beyond graphene. *ACS Nano* **2013**, *7*, 2898–2926. [CrossRef]
3. Srivastava, M.; Banerjee, S.; Bairagi, S.; Singh, P.; Kumar, B.; Singh, P.; Kale, R.D.; Mulvihill, D.M.; Ali, S.W. Recent progress in molybdenum disulfide (MoS_2) based flexible nanogenerators: An inclusive review. *Chem. Eng. J.* **2024**, *480*, 147963. . [CrossRef]
4. Kormányos, A.; Zólyomi, V.; Drummond, N.D.; Burkard, G. Spin-Orbit Coupling, Quantum Dots, and Qubits in Monolayer Transition Metal Dichalcogenides. *Phys. Rev. X* **2014**, *4*, 011034. [CrossRef]
5. Wang, Y.; Cong, C.; Qiu, C.; Yu, T. Raman Spectroscopy Study of Lattice Vibration and Crystallographic Orientation of Monolayer MoS_2 under Uniaxial Strain. *Small* **2013**, *9*, 2857–2861. [CrossRef] [PubMed]
6. Nickel, R.; Gibbs, J.; Burgess, J.; Shafer, P.; Meira, D.M.; Sun, C.; van Lierop, J. Nanoscale size effects on push–pull Fe–O hybridization through the multiferroic transition of perovskite ϵ-Fe_2O_3. *Nano Lett.* **2023**, *23*, 7845–7851. [CrossRef]

7. Hoque, A.M.; Rahman, M.; Islam, M.R.; Hossain, M.; Yamamoto, M. Spin–Valley Coupling and Spin-Relaxation Anisotropy in All-CVD Graphene–MoS_2 van der Waals Heterostructure. *Phys. Rev. Mater.* **2023**, *7*, 044005. [CrossRef]
8. Rani, A.; Verma, A.; Yadav, B.C. Advancements in transition metal dichalcogenides (TMDCs) for self-powered photodetectors: Challenges, properties, and functionalization strategies. *Mater. Adv.* **2024**, *5*, 3535–3562. [CrossRef]
9. Xu, J.; Zheng, Q.; Zhao, J. Spontaneous polarization dynamics in V-doped monolayer MoS_2. *Comput. Mater. Today* **2024**, *1*, 100004. [CrossRef]
10. Chan, C.-W.; Hsieh, C.-Y.; Chan, F.-M.; Yang, C.-Y. Valley Spin–Polarization of MoS_2 Monolayer Induced by Ferromagnetic Order in an Antiferromagnet. *Materials* **2024**, *17*, 3933. [CrossRef]
11. Aghoutane, N.; Feddi, E.; El-Yadri, M.; Bailach, J.B.; Dujardin, F.; Duque, C.A. Magnetic field and dielectric environment effects on an exciton trapped by an ionized donor in a spherical quantum dot. *Superlattices Microstruct.* **2017**, *111*, 1082–1092. [CrossRef]
12. Vinasco, J.A.; Londoño, M.A.; Restrepo, R.L.; Mora-Ramos, M.E.; Feddi, E.; Radu, A.; Kasapoglu, E.; Morales, A.L.; Duque, C.A. Optical absorption and electroabsorption related to electronic and single dopant transitions in holey elliptical GaAs quantum dots. *Phys. Status Solidi B* **2018**, *255*, 1700470. [CrossRef]
13. Ospina, D.A.; Cisternas, E.; Duque, C.A.; Correa, J.D. Electronic structure and STM image simulation of defects on hBN/black-phosphorene heterostructures: A theoretical study. *Surf. Sci.* **2018**, *669*, 95–102. [CrossRef]
14. Ospina, D.A.; Duque, C.A.; Mora-Ramos, M.E.; Correa, J.D. Theoretical study of phosphorene multilayers: Optical properties and small organic molecule physisorption. *J. Mater. Sci.* **2018**, *53*, 5103–5113. [CrossRef]
15. Ortakaya, S.; Hammouda, K.; Zeiri, N.; Duque, C.A. Excitonic phenomena in the multilayer QDs: Perturbative approach. *Phys. Lett. A* **2025**, *544*, 130474. [CrossRef]
16. Splendiani, A.; Sun, L.; Zhang, Y.; Li, T.; Kim, J.; Chim, C.-Y.; Wang, F. Emerging Photoluminescence in Monolayer MoS_2. *Nano Lett.* **2010**, *10*, 1271–1275. [CrossRef]
17. Kuc, A.; Zibouche, N.; Heine, T. Influence of Quantum Confinement on the Electronic Structure of the Transition Metal Sulfide TS_2. *Phys. Rev. B* **2011**, *83*, 245213. [CrossRef]
18. Dolui, K.; Rungger, I.; Das Pemmaraju, C.; Sanvito, S. Possible Doping Strategies for MoS_2 Monolayers: An ab initio Study. *Phys. Rev. B* **2013**, *88*, 075420. [CrossRef]
19. Ramasubramaniam, A.; Naveh, D.; Towe, E. Tunable Band Gaps in Bilayer Transition-Metal Dichalcogenides. *Phys. Rev. B* **2011**, *84*, 205325. [CrossRef]
20. Li, Q.; Zhao, X.; Deng, L.; Peng, B.; Zhang, Y.; Wang, Z.; Wang, L.; Wang, X.; Zhang, H.; Zhu, H.; et al. Enhanced valley Zeeman splitting in Fe-doped monolayer MoS_2. *ACS Nano* **2020**, *14*, 4636–4645. [CrossRef] [PubMed]
21. Xie, L.; Wang, X.; Lu, J.; Ni, Z.; Luo, Z.; Mao, H.; Wang, R.; Wang, Y.; Huang, H.; Qi, D.; et al. Room temperature ferromagnetism in partially hydrogenated epitaxial graphene. *Appl. Phys. Lett.* **2011**, *98*, 193113. [CrossRef]
22. Hossen, M.F.; Shendokar, S.; Aravamudhan, S. Defects and defect engineering of two-dimensional transition metal dichalcogenide (2D TMDC) materials. *Nanomaterials* **2024**, *14*, 410. [CrossRef]
23. Afrid, S.M.T. Defect-Engineered Magnetism Induction and Electronic Structure Modulation in Monolayer MoS_2. *Heliyon* **2024**, *10*, e23384. [CrossRef] [PubMed]
24. Komsa, H.-P.; Krasheninnikov, A.V. Engineering the electronic properties of two-dimensional transition metal dichalcogenides by introducing mirror twin boundaries. *Adv. Electron. Mater.* **2017**, *3*, 1600468. [CrossRef]
25. Baithi, M.; Duong, D.L. Doped, two-dimensional, semiconducting transition metal dichalcogenides in low-concentration regime. *Crystals* **2024**, *14*, 832. [CrossRef]
26. Zhou, W.; Zou, X.; Najmaei, S.; Liu, Z.; Shi, Y.; Kong, J.; Idrobo, J.-C. Intrinsic Structural Defects in Monolayer Molybdenum Disulfide. *Nano Lett.* **2013**, *13*, 2615–2622. [CrossRef]
27. Brennan, C.J.; Ghosh, R.; Koul, K.; Banerjee, S.K.; Lu, N.; Yu, E.T. Out-of-Plane Electromechanical Response of Monolayer Molybdenum Disulfide Measured by Piezoresponse Force Microscopy. *Nano Lett.* **2017**, *17*, 5464–5471. [CrossRef]
28. Liu, W.; Kang, J.; Sarkar, D.; Khatami, Y.; Jena, D.; Banerjee, K. Role of metal contacts in designing high-performance monolayer n-type WSe_2 field effect transistors. *Nano Lett.* **2013**, *13*, 1983–1990. [CrossRef]
29. Tongay, S.; Varnoosfaderani, S.S.; Appleton, B.R.; Wu, J.; Hebard, A.F. Magnetic properties of MoS_2: Existence of ferromagnetism. *Appl. Phys. Lett.* **2012**, *101*, 123105. [CrossRef]
30. Gentili, D.; Calabrese, G.; Lunedei, E.; Borgatti, F.; Mirshokraee, S.A.; Benekou, V.; Tseberlidis, G.; Mezzi, A.; Liscio, F.; Candini, A.; et al. Tuning Electronic and Functional Properties in Defected MoS_2 Films by Surface Patterning of Sulfur Atomic Vacancies. *Small Methods* **2025**, *9*, 2401486. [CrossRef] [PubMed]
31. Kresse, G.; Furthmüller, J. Efficient Iterative Schemes for Ab Initio Total-Energy Calculations Using a Plane-Wave Basis Set. *Phys. Rev. B* **1996**, *54*, 11169–11186. [CrossRef]
32. Yoshimura, A.; Koratkar, N.; Meunier, V. Substitutional transition metal doping in MoS_2: A first-principles study. *Nano Express* **2020**, *1*, 010008. [CrossRef]

33. Liu, J.; Zhang, X.; Lu, G. Excitonic Effect Drives Ultrafast Dynamics in van der Waals Heterostructures. *Nano Lett.* **2020**, *20*, 4048–4054. [CrossRef]
34. Casida, M.E. Time-Dependent Density Functional Response Theory for Molecules. In *Recent Developments and Applications of Modern Density Functional Theory*; Seminario, J.M., Ed.; Elsevier: Amsterdam, The Netherlands, 1996; Volume 4, pp. 391–439. [CrossRef]
35. Ge, M.; Wang, H.; Wu, J.; Si, C.; Zhang, J.; Zhang, S. Enhanced Valley Splitting of WSe_2 in Twisted van der Waals WSe_2/CrI_3 Heterostructures. *npj Comput. Mater.* **2022**, *8*, 32. [CrossRef]
36. Farkous, M.; Bikerouin, M.; Thuan, D.V.; Benhouria, Y.; El-Yadri, M.; Feddi, E.; Erguig, H.; Dujardin, F.; Nguyen, C.V.; Hieu, N.V.; et al. Strain Effects on the Electronic and Optical Properties of van der Waals Heterostructure MoS_2/WS_2: A First-Principles Study. *Phys. E Low-Dimens. Syst. Nanostruct.* **2020**, *116*, 113799. [CrossRef]
37. Farkous, M.; Bikerouin, M.; Phung, H.T.T.; El-Yadri, M.; Feddi, E.; Dujardin, F.; Duque, C.A.; Muoi, D.; Phuc, H.V.; Nguyen, C.V.; et al. Electronic and Optical Properties of Layered van der Waals Heterostructure Based on MS_2 (M = Mo, W) Monolayers. *Mater. Res. Express* **2019**, *6*, 065060. [CrossRef]
38. Wang, Y.; Li, S.; Yi, J. Electronic and Magnetic Properties of Co-Doped MoS_2 Monolayer. *Sci. Rep.* **2016**, *6*, 24153. [CrossRef] [PubMed]
39. Ataca, C.; Sahin, H.; Ciraci, S. Stable, Single-Layer MX_2 Transition-Metal Oxides and Dichalcogenides in a Honeycomb-Like Structure. *J. Phys. Chem. C* **2012**, *116*, 8983–8999. [CrossRef]
40. Liu, J.; Lu, G.; Zhang, X. Exciton Dispersion and Exciton–Phonon Interaction in Solids by Time-Dependent Density Functional Theory. *J. Chem. Phys.* **2023**, *158*, 044116. [CrossRef]
41. Ouma, C.N.M.; Singh, S.; Obodo, K.O.; Amolo, G.O.; Romero, A.H. Controlling the Magnetic and Optical Responses of a MoS_2 Monolayer by Lanthanide Substitutional Doping: A First-Principles Study. *Phys. Chem. Chem. Phys.* **2017**, *19*, 25555–25563. [CrossRef]
42. Qiu, D.Y.; da Jornada, F.H.; Louie, S.G. Screening and Many-Body Effects in Two-Dimensional Crystals: Monolayer MoS_2. *Phys. Rev. B* **2016**, *93*, 235435. [CrossRef]
43. Mak, K.F.; Lee, C.; Hone, J.; Shan, J.; Heinz, T.F. Atomically Thin MoS_2: A New Direct-Gap Semiconductor. *Phys. Rev. Lett.* **2010**, *105*, 136805. [CrossRef]
44. Ma, Y.; Dai, Y.; Guo, M.; Niu, C.; Zhu, Y.; Huang, B. Evidence of the Existence of Magnetism in Pristine VX_2 Monolayers (X = S, Se) and Their Strain-Induced Tunable Magnetic Properties. *ACS Nano* **2012**, *6*, 1695–1701. [CrossRef]
45. Mishra, R.; Zhou, W.; Pennycook, S.J.; Pantelides, S.T.; Idrobo, J.-C. Long-Range Ferromagnetic Ordering in Manganese-Doped Two-Dimensional Dichalcogenides. *Phys. Rev. B* **2013**, *88*, 144409. [CrossRef]